

A theoretical study of multidimensional nuclear tunneling in malonaldehyde

Norihiro Shida, Paul F. Barbara, and Jan E. Almlöf

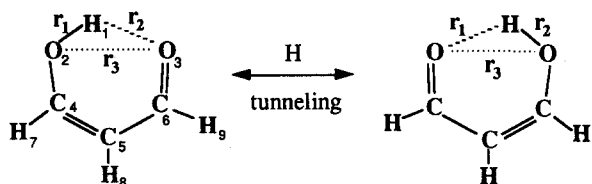
Department of Chemistry, University of Minnesota, S. E. Minneapolis, Minnesota 55455

(Received 6 March 1989; accepted 14 June 1989)

Various aspects of the intramolecular proton transfer in malonaldehyde have been investigated theoretically within the reaction surface Hamiltonian framework, which was recently applied with a two-dimensional surface to this molecule by Carrington and Miller. The present calculation, which involves a three-dimensional reaction surface and a high level of *ab initio* accuracy, gives a tunneling splitting which is $\sim 50\%$ smaller than experiment and a hydrogen/deuterium isotope effect that is within 40% of experiment with no adjustable parameter. The vibrational wave function has been analyzed to extract an effective curvilinear tunneling path on the hypersurface. The path calculations, and other analysis, clearly demonstrate the limitations of one-dimensional models for polyatomic tunneling systems like malonaldehyde. In addition, tunneling splittings have been calculated for excited vibrational states of malonaldehyde, leading to new insight into the multidimensional character of proton transfer.

I. INTRODUCTION

Malonaldehyde (MA) and related molecules have been used as important prototypes for the theoretical¹⁻⁹ and experimental¹⁰⁻¹³ investigation of proton tunneling in polyatomic systems.



Nuclear tunneling between the two equivalent isomers of MA has experimental manifestations in microwave and far infrared spectroscopy which can be analyzed to yield a $\sim 21 \text{ cm}^{-1}$ tunneling splitting of the ground vibrational state of MA, and a $\sim 3 \text{ cm}^{-1}$ splitting for the H_1 deuterated species.¹⁰

A straightforward calculation of the tunneling splitting would amount to first determining a 21-dimensional Born-Oppenheimer potential surface, then solving for the lowest pair of vibrational states in that potential. Since the surface is strongly anharmonic, analytic derivative methods are of little use, and such a calculation would be beyond our computational capability at present.

A number of different approximate approaches have been taken to make the calculation of the splitting practical. Over a decade ago, Fluder and de la Vega calculated the splitting employing a rudimentary, one-dimensional double minimum potential.^{5(a),5(b)} The model potential was fit to *ab initio* SCF energies of a few geometries near the equilibrium geometry and saddle point (i.e., conventional transition state). The calculated splitting was only 0.75 cm^{-1} , almost two orders of magnitude smaller than experiment. They also considered alternative one-dimensional paths for nuclear tunneling, and found that tunneling along the minimum energy path was inefficient because the minimum energy path involves large motion of heavy atoms. Other paths having

pure hydrogen motions gave a much larger splitting, although still almost an order of magnitude smaller than the experimental value. The Fluder and de la Vega calculation did not consider the effect of the multicoordinate vibrational motion of MA on the tunneling coordinate.

In 1983, Bicerano *et al.* made an improved one-dimensional calculation of the splitting that employed an accurate SCF-CI (self-consistent field-configuration interaction) determination of the barrier energy V_0 and vibrational frequencies (ω) of the normal modes of MA in the equilibrium (ω_k) and barrier geometries (ω_k^\ddagger).^{5(c)} The calculation assumed that the tunneling path was a pure O-H stretching motion and the effect of the "orthogonal" vibrational modes was treated adiabatically. The WKB approximation was used to calculate the splitting, and therefore only the equilibrium and barrier geometries needed to be considered explicitly. According to this model, the effective barrier energy V_{eff} for the ground vibrational level is given by

$$V_{\text{eff}} = V_0 + \sum_{\alpha=1}^{F-1} \frac{1}{2}(\omega_{\alpha}^{\ddagger} - \omega_{\alpha}), \quad (1.1)$$

where $F = 3N - 6$, i.e., 21 for MA. The adiabatic one-dimensional treatment can be justified on the assumption that the $3N - 7$ orthogonal vibrational degrees of freedom can rapidly (adiabatically) adjust as the proton tunneling motion occurs.

The choice of a path for a chemical reaction is a complex issue that has been investigated for many years.¹⁴⁻¹⁶ One unique choice for the path is Fukui's well-known Intrinsic Reaction Coordinate (IRC).^{14(a)-14(c)} This is an inefficient tunneling path for MA,⁵ or for any "heavy-light-heavy" system, because it includes too much motion of heavy atoms.⁶ Instead, the choice of path made by Bicerano *et al.*^{5(c)} and, independently, by Fluder *et al.*^{5(a)} emphasized O-H stretching motion. The one-dimensional treatments just described are closely related to the reaction path methods for vibrational structure and dynamics, which have been successfully applied in many cases.¹⁵⁻¹⁷ The simplest and best defined case is the IRC path in the Born-Oppenheimer potential energy surface. The IRC is uniquely defined as the

steepest descent path from the saddle point on the PES to the equilibrium geometry in mass-weighted Cartesian coordinates.¹⁴ The PES forms a valley around this path, i.e., at each point (r) along the IRC, there are $3N - 7$ orthogonal directions expressed as the local normal modes (Q), such that

$$\left[\frac{\partial V(r, Q)}{\partial Q_\alpha} \right]_{Q=0} = 0, \quad (1.2a)$$

$$\left[\frac{\partial^2 V(r, Q)}{\partial Q_\alpha \partial Q_\beta} \right]_{Q=0} = \omega_\alpha^2 \delta_{\alpha\beta}. \quad (1.2b)$$

If the orthogonal degrees of freedom (sometimes called the bath) are treated quadratically, $V(r, Q_0)$ together with the $3N - 7$ $\omega_\alpha(r)$ and Q_α gives a local representation of the PES along the path r .¹⁵ Assuming further that the bath modes can rapidly adjust to changes in r , the effect of the bath modes can be treated adiabatically giving the approximate expressions for the effective one-dimensional potential $V_{\text{eff}}(r)$ along the IRC,

$$V_{\text{eff}}(r) = V(r) + \frac{1}{2} \sum_{\alpha=1}^{3N-7} \omega_\alpha^2(r). \quad (1.3)$$

One complication in applying this to double-minimum tunneling problems in polyatomics is that the IRC is entirely undefined on the side of the minimum energy geometry opposite to the direction of the saddle point. In a later section of this paper, we give a practical solution to this problem, by employing the gradient extremal algorithm for finding the unknown position of the path.^{18,19}

Miller and co-workers have argued that the MA molecule is a polyatomic version of a heavy-light-heavy mass combination reaction, as such the IRC path should not be a good representation of the actual reaction path.⁵⁻⁷ In particular, for MA the heavy motion is primarily "stretching" motion between the two oxygen atoms. This is the initial main character of the IRC as the molecule moves from the equilibrium geometry to the saddle point.¹⁻⁹ Near the saddle point the IRC is primarily hydrogenic motion. The IRC is, therefore, sharply curved and the actual dynamical motion must deviate from the IRC. The O-H stretching path employed by Bicerano *et al.* represents an alternative (non-IRC) path for the nuclear tunneling.^{5(c)}

A. Reaction surface description

A major breakthrough on the MA problem was reported in 1986 by Carrington and Miller.⁷ They modeled the intramolecular proton transfer with an adiabatic reaction surface Hamiltonian. The proton tunneling splitting was calculated solving a two-dimensional nuclear Schrödinger equation for an effective two-dimensional potential energy surface with the two O-H bond lengths r_1 and r_2 as the coordinates. The effective reaction surface $V(r_1, r_2)$ was constructed from the bare potential surface $V_0(r_1, r_2)$ and a simple adiabatic term $\sum_{\alpha=1}^{3N-8} \frac{1}{2} \omega_\alpha^2(r_1, r_2)$. Thus the dynamics of the large amplitude degrees of freedom are treated in detail in the two-dimensional space while the motion of the bath modes are treated adiabatically and assumed to be locally harmonic.

Ideally, the surface is found by solving the electronic problem at each r_1, r_2 point with the $3N - 8$ remaining de-

grees of freedom (bath modes) varied to yield the minimum $V(r_1, r_2)$. The vibrational frequencies of the bath modes $\omega_\alpha(r_1, r_2)$ are found by expanding the potential quadratically about the minimized and constrained (r_1, r_2) geometry.

The reaction surface method has several key differences from the one-dimensional treatments. For example, compared to the minimum energy reaction path approach, the reaction surface description allows for dynamics and tunneling far from the IRC. Another difference is that the choice of the reaction surface coordinates made by Carrington and Miller was based on intuition (using the most obvious choice for two large amplitude degrees of freedom) rather than a unique mathematical procedure such as the one-dimensional IRC path. A number of other approaches to the modeling of tunneling far from the IRC, such as the large curvature approximation methods, have been reported.¹⁶

Determining the reaction surface is much more computationally intensive than one-dimensional treatments in general, and, in particular, the simple WKB approach. Furthermore, recent high-level electronic calculations on MA have demonstrated the necessity to include electron correlation effects if energies and geometries accurate enough for proton tunneling calculations are to be obtained. In order to make the *ab initio* calculation of the reaction surface tractable, Carrington and Miller first calculated the two-dimensional reaction surface and bath frequencies at the SCF level with a minimum basis set. The surface was improved by scaling the polynomial so that the geometries and energies of the equilibrium point and saddle point agreed with the previously published *ab initio* calculation of MA that went beyond the SCF level, i.e., MP2 and MP4.⁸ Vibrational frequencies of the bath were calculated at the SCF level.

Employing the effective two-dimensional reaction surface potential energy surface (which has a classical barrier of 4.3 kcal/mol), Carrington and Miller calculated a tunneling splitting of 60 cm^{-1} , which is about a factor of 3 larger than experiment. A tunneling splitting in agreement with experiment was obtained by linearly scaling the reaction surface such that the classical barrier was increased to 6.8 kcal/mol.

B. Motivation and overview

The reaction surface Hamiltonian approach is a straightforward procedure to calculate vibrational wave functions and energy levels (yielding tunneling splitting) for polyatomics. It is also an excellent framework for exploring complex multidimensional tunneling effects. It is important to test the accuracy of this procedure with respect to experiment and the sensitivity of this calculation to the choice of surface variables which is somewhat arbitrary. The availability of enhanced *ab initio* methods (that take advantage of the most powerful computers and new algorithms for analytically determining first and second derivatives of the potential with respect to nuclear displacement) has allowed us to make a considerably enhanced reaction surface calculation for MA that involves a three-dimensional surface and a more exact and extensive electronic calculation of the shape of the reaction surface. This calculation is the subject of this paper.

Our reaction surface is a function of three coordinates,

the two O–H distances r_1 , r_2 , and the O–O distance. This allows for complex large amplitude motion involving the O–H bending motions, O–H stretching motion, and the displacement of the O–O distance (r_3). The latter two motions are major components of the IRC for MA.

Section II outlines our alternative derivation of the reaction surface Hamiltonian. The result is mathematically equivalent to that of Carrington and Miller, but the derivation is more straightforward. In this section, we also describe the potential surface calculation, including the details of the *ab initio* electronic structure calculation.

In Sec. III we compare the calculated tunneling splitting to experiment. In addition, we use the new reaction surface Hamiltonian calculations to explore several key aspects of polyatomic nuclear tunneling, including hydrogen/deuterium isotope effects, nuclear tunneling paths, one-dimensional IRC models, and tunneling of excited vibrational states.

II. METHOD OF CALCULATION

A. Reaction surface Hamiltonian

This section describes our implementation of the reaction surface Hamiltonian method by Carrington and Miller.⁷ Our approach emphasizes the use of Cartesian coordinates, as opposed to internal coordinates which were used in Carrington and Miller's derivation. Our implementation leads to a simpler and more straightforward computational algorithm, since we emphasize Cartesian coordinates which are the common coordinates for *ab initio* computer codes.

Assume that an arbitrary point \mathbf{X} in a molecule fixed mass-weighted Cartesian coordinate system can be expressed in terms of reaction surface (internal) coordinates \mathbf{r} and bath coordinates \mathbf{Q} as

$$X_i = [S_i(\mathbf{r}) + L_{i\alpha}(\mathbf{r})Q_\alpha], \quad (2.1a)$$

$$\mathbf{X} = \{\sqrt{m_1}x_1, \sqrt{m_1}y_1, \sqrt{m_1}z_1, \dots, \sqrt{m_N}z_N\}, \quad (2.1b)$$

where (x_i, y_i, z_i) is the position of atom i in Cartesian coordinates, m_i is the nuclear mass of atom i , and m is the dimensionality of the reaction surface. $\mathbf{S}(\mathbf{r})$ is the reaction surface expressed in terms of mass-weighted Cartesian coordinates. $\mathbf{L}(\mathbf{r})$ transforms small displacements of the bath coordinates to mass-weighted Cartesian coordinates. Both \mathbf{L} and \mathbf{S} will be discussed in detail below. We have adopted Einstein's summation rule²⁰ and always use the following running suffixes:

$i, j: 1 \sim 3N$ (suffixes of mass-weighted Cartesian coordinates),

$k, l: 1 \sim m$ (suffixes of reaction surface coordinates),

$\alpha, \beta, \gamma: 1 \sim 3N - 6 - m$ (suffixes of bath coordinates).

The reaction surface coordinate r_k is a function of \mathbf{X} , i.e., the following inverse relation exists;

$$r_k = F_k(\mathbf{X}). \quad (2.2)$$

Before deriving an explicit form for the reaction surface Hamiltonian, we obtain an expression for the classical kinetic energy \hat{T} in terms of \mathbf{r} , \mathbf{Q} , and the conjugate momenta \mathbf{P}_r and \mathbf{P}_Q .

$$\hat{T}(\mathbf{r}, \mathbf{Q}, \mathbf{P}_r, \mathbf{P}_Q) = (\mathbf{P}_r^T \mathbf{P}_Q^T) \begin{pmatrix} \mathbf{G}_{rr} & \mathbf{G}_{rQ} \\ \mathbf{G}_{Qr} & \mathbf{G}_{QQ} \end{pmatrix} \begin{pmatrix} \mathbf{P}_r \\ \mathbf{P}_Q \end{pmatrix}. \quad (2.3)$$

\mathbf{G} , the so-called Wilson's \mathbf{G} matrix,²¹ is defined as

$$G_{qq'} = \frac{\partial q}{\partial X_i} \frac{\partial q'}{\partial X_i}. \quad (2.4)$$

The formal expression of the \mathbf{G} matrix can be obtained as follows: The derivatives of \mathbf{r} and \mathbf{Q} with respect to \mathbf{X} are calculated from the relations in Eqs. (2.1) and (2.2) as

$$\frac{\partial r_k}{\partial X_i} = \frac{\partial F_k(\mathbf{X})}{\partial X_i}, \quad (2.5a)$$

$$\begin{aligned} \frac{\partial Q_\alpha}{\partial X_i} &= \frac{\partial F_k(\mathbf{X})}{\partial X_i} \frac{\partial L_{j\alpha}(\mathbf{r})}{\partial r_k} [X_j - S_j(\mathbf{r})] \\ &\quad + L_{j\alpha}(\mathbf{r}) \left[\delta_{ij} - \frac{\partial F_k(\mathbf{X})}{\partial X_i} \frac{\partial S_j(\mathbf{r})}{\partial r_k} \right] \\ &= \frac{\partial F_k(\mathbf{X})}{\partial X_i} \frac{\partial L_{j\alpha}(\mathbf{r})}{\partial r_k} L_{j\beta}(\mathbf{r}) Q_\beta \\ &\quad + L_{j\alpha}(\mathbf{r}) \left[\delta_{ij} - \frac{\partial F_k(\mathbf{X})}{\partial X_i} \frac{\partial S_j(\mathbf{r})}{\partial r_k} \right]. \end{aligned} \quad (2.5b)$$

The \mathbf{G} matrix in Eq. (2.3) is now determined from Eqs. (2.4) and (2.5) as

$$G_{kl}^{(k,l=\{r\})} = \frac{\partial F_k}{\partial X_i} \frac{\partial F_l}{\partial X_i}, \quad (2.6a)$$

$$\begin{aligned} G_{\alpha\beta}^{(\alpha,\beta=\{Q\})} &= L_{i\alpha} \left(1 - \frac{\partial S_i}{\partial r_k} \frac{\partial F_k}{\partial X_j} - \frac{\partial F_k}{\partial X_i} \frac{\partial S_j}{\partial r_k} \right. \\ &\quad \left. + \frac{\partial S_i}{\partial r_k} G_{kl} \frac{\partial S_j}{\partial r_l} \right) L_{j\beta}, \end{aligned} \quad (2.6b)$$

$$\begin{aligned} G_{k\alpha}^{(k=\{r\}, \alpha=\{Q\})} &= G_{\alpha k} = G_{kl} \left[\frac{\partial L_{i\alpha}}{\partial r_l} L_{i\beta} Q_\beta - L_{i\alpha} \frac{\partial S_i}{\partial r_l} \right] \\ &\quad + \frac{\partial F_k}{\partial X_i} L_{i\alpha}, \end{aligned} \quad (2.6c)$$

where terms of third and higher order in \mathbf{Q} are neglected to obtain a consistent level of the approximation. [In our scheme, the last term in Eq. (2.6c) is always zero because of the conditions we impose on the \mathbf{Q} which are described below (also see Appendix 1).]

The reaction surface Hamiltonian of this form is written using the \mathbf{G} matrix in Eq. (2.6) as

$$\begin{aligned} \hat{H}(\mathbf{r}, \mathbf{p}_r, \mathbf{Q}, \mathbf{p}_Q) &= \frac{1}{2} (\mathbf{p}_r^T \mathbf{p}_Q^T) \begin{pmatrix} \mathbf{G}_{rr} & \mathbf{G}_{rQ} \\ \mathbf{G}_{Qr} & \mathbf{G}_{QQ} \end{pmatrix} \begin{pmatrix} \mathbf{p}_r \\ \mathbf{p}_Q \end{pmatrix} \\ &\quad + V_0(\mathbf{r}) + \frac{1}{2} \omega_\alpha^2(\mathbf{r}) Q_\alpha^2, \end{aligned} \quad (2.7)$$

where it is assumed that the reaction surface is the minimum energy surface.

To construct the minimum energy surface, the following condition must be fulfilled at each point on the reaction surface $\mathbf{S}(\mathbf{r})$;

$$\left[\frac{\partial V(\mathbf{r}, \mathbf{Q})}{\partial \mathbf{Q}} \right]_{\mathbf{r}=\mathbf{r}, \mathbf{Q}=\mathbf{0}} = \mathbf{0}. \quad (2.8)$$

Up to this point, Eq. (2.8) can not be evaluated since \mathbf{Q} has

not yet been uniquely determined. Here, we impose the following condition on \mathbf{Q} :

$$\frac{\partial r_k}{\partial X_i} \frac{\partial Q_\alpha}{X_i} = \frac{\partial r_k}{\partial X_i} L_{i\alpha} = 0. \quad (2.9)$$

Equation (2.9) enforces the orthogonality between the reaction coordinates \mathbf{r} and the bath normal coordinates \mathbf{Q} [Note that the \mathbf{Q} 's are not orthogonal to the reaction surface $\mathbf{S}(\mathbf{r})$]. Using Eq. (2.9), the minimum surface condition (2.8) can be obtained in a mass-weighted Cartesian coordinate system as (see Appendix 1):

$$\{\mathbf{1} - \mathcal{P}^{(r)}[\mathbf{S}(\mathbf{r})]\} \mathbf{g}_X[\mathbf{S}(\mathbf{r})] = \mathbf{0}, \quad (2.10)$$

where \mathbf{g}_X is the gradient vector in a mass-weighted Cartesian coordinate system defined as

$$[\mathbf{g}_X(\mathbf{X})]_i = \frac{\partial V(\mathbf{X})}{\partial X_i}. \quad (2.11)$$

$\mathcal{P}^{(r)}$ is the projection operator which projects an arbitrary vector onto \mathbf{r} space;

$$\mathcal{P}^{(r_k)}(\mathbf{X}) = \left[\left| \frac{\partial F_k(\mathbf{X})}{\partial \mathbf{X}} \right\rangle \left\langle \frac{\partial F_k(\mathbf{X})}{\partial \mathbf{X}} \right| \right] / \left[\left\langle \frac{\partial F_k(\mathbf{X})}{\partial \mathbf{X}} \left| \frac{\partial F_k(\mathbf{X})}{\partial \mathbf{X}} \right\rangle \right], \quad (2.12a)$$

$$(\mathbf{1} - \mathcal{P}^{(r)}) = (\mathbf{1} - \mathcal{P}^{(r_1)})(\mathbf{1} - \mathcal{P}^{(r_2)}) \dots (\mathbf{1} - \mathcal{P}^{(r_m)}). \quad (2.12b)$$

The adiabatic Hamiltonian⁷ can be obtained by neglecting the off-diagonal couplings in Eq. (2.7) as

$$\hat{H}(\mathbf{r}, \mathbf{p}_r) = \frac{1}{2} \mathbf{p}_r^T \mathbf{G}_{rr}(\mathbf{r}) \mathbf{p}_r + V_0(\mathbf{r}) + \sum_\alpha \frac{1}{2} \bar{\omega}_\alpha(\mathbf{r}). \quad (2.13)$$

Since $\mathbf{G}_{\mathbf{Q}\mathbf{Q}}$ in Eq. (2.6b) is not the unit matrix, the local normal frequencies ($\bar{\omega}$) in Eq. (2.13) are obtained in close analogy with Wilson's GF matrix method²⁰ as follows;

$$(\mathbf{G}_{\mathbf{Q}\mathbf{Q}})_{\alpha\beta} \bar{\omega}_\beta^2 \bar{\Lambda}_{\beta\gamma} = \bar{\omega}_\alpha^2 \bar{\Lambda}_{\alpha\gamma}. \quad (2.14)$$

$\partial \mathbf{S} / \partial \mathbf{r}$ and \mathbf{L} in Eq. (2.6b) can be calculated as follows.

When the minimum surface condition (2.10) is fulfilled at every point in $\mathbf{S}(\mathbf{r})$, the following relation must be also satisfied.

$$\frac{d}{dr_k} \{\mathbf{1} - \mathcal{P}(\mathbf{r})[\mathbf{S}(\mathbf{r})]\} \mathbf{g}_X[\mathbf{S}(\mathbf{r})] = 0. \quad (2.15)$$

Since, in general,

$$\frac{d}{dx} A[B(x)] = \left[\frac{\partial A(y)}{\partial y} \right]_{y=B(x)} \frac{\partial B(x)}{\partial x}, \quad (2.16)$$

the condition in Eq. (2.15) can be evaluated as

$$\left\{ [(\mathbf{1} - \mathcal{P}(\mathbf{r})) \mathbf{H}_X]_{ij} - \left(\frac{\partial \mathcal{P}^{(r)}}{\partial X_j} \mathbf{g}_X \right)_i \right\} \frac{\partial S_j}{\partial r_k} = 0, \quad (2.17)$$

where \mathbf{H}_X is the nuclear Hessian matrix in a mass-weighted Cartesian coordinate system defined as

$$[\mathbf{H}_X(\mathbf{X})]_{ij} = \frac{\partial^2 V(\mathbf{X})}{\partial X_i \partial X_j}. \quad (2.18)$$

In Eq. (2.17), only $(3N - 6 - m)$ of the equations are linearly independent for each r_k . To determine the $\partial \mathbf{S} / \partial r_k$, additional $m + 6$ equations are required. They are

$$\frac{\partial F_1}{\partial X_j} \frac{\partial S_j}{\partial r_k} = \delta_{kl}, \quad (2.19a)$$

$$\mathcal{P}_j^{(\lambda)} \frac{\partial S_j}{\partial r_k} = 0, \quad (\lambda = 1-3), \quad (2.19b)$$

$$\mathcal{G}_j^{(\lambda)} \frac{\partial S_j}{\partial r_k} = 0, \quad (\lambda = 1-3), \quad (2.19c)$$

where \mathcal{P} and \mathcal{G} are vectors describing infinitesimal rotations and translations, respectively. $\partial \mathbf{S} / \partial r_k$ can now be obtained by solving the linear equations of Eqs. (2.17) and (2.19).

Finally, \mathbf{L} in Eq. (2.6) and ω in Eq. (2.7) can be calculated as follows (more details are given in Appendix 1):

$$(\mathbf{H}'_{\text{eff}})_{ij} L_{j\alpha} = \omega_\alpha^2 L_{i\alpha} \quad (2.20a)$$

$$\mathbf{H}'_{\text{eff}} = (\mathbf{1} - \mathcal{P}) \mathbf{H}_{\text{eff}} (\mathbf{1} - \mathcal{P}), \quad (2.20b)$$

$$(\mathbf{H}_{\text{eff}})_{ij} \equiv (\mathbf{H}_X)_{ij} - \frac{\partial^2 r_k}{\partial X_i \partial X_j} (\mathbf{g}_r)_k, \quad (2.20c)$$

where \mathbf{g}_r is the gradient vector in terms of reaction coordinates \mathbf{r} , and $(\mathbf{1} - \mathcal{P})$ is the projection operator which projects out the rotational, translational, and \mathbf{r} components from an arbitrary vector. \mathbf{H}_{eff} is the effective Hessian matrix in mass-weighted Cartesian coordinates. Note that \mathbf{H}_{eff} is explicitly dependent on \mathbf{g}_r [second term in Eq. (2.20c)] as a result of the nonlinear transformation between mass-weighted Cartesian coordinates and internal coordinates.

B. Potential energy surface and vibrational calculations

The procedure we employ to construct the three-dimensional potential energy surface combines *ab initio* SCF calculations and *ab initio* SCF-MCPF (Modified Coupled Pair Functional) calculations.²² The latter calculations include higher order dynamic correlation effects in a size consistent way, yielding a surface with an accurate shape and barrier energy.

The starting point of the construction of the surface is an SCF calculation using the following basis set functions. (i) $(7s3p)$ contracted to $[4s2p]$ on carbon and oxygen²³; (ii) $(4s)$ contracted to $[2s]$ on hydrogen²³; (iii) d type polarization function (orbital exponent, $\alpha = 0.85$) on oxygen; and (iv) a p type polarization function ($\alpha = 1.0$) on the tunneling proton. Constrained geometry optimization was performed at 89 different geometries \mathbf{r} according to the conditions defined by Eq. (2.10).

At each optimized geometry the $3N$ dimensional gradient vector and the $3N \times 3N$ Hessian matrix was calculated in mass-weighted Cartesian coordinates. The vibrational frequencies of the local normal modes were calculated by the method outlined above.

The SCF energy and gradient vectors at the 89 geometries were fit by a sixth order polynomial representation of the surface, $V^{\text{SCF}}(\mathbf{r})$. A polynomial representation of the zero point energy of the bath (at the SCF level) $\text{ZPE}^{\text{SCF}}(\mathbf{r})$ was determined by fitting $\frac{1}{2} \sum_{\alpha=1}^{3N-9} \bar{\omega}_\alpha(\mathbf{r})$ as a function of \mathbf{r} to fourth order.

A correlation correction to the SCF potential energy surface was determined from MCPF calculations made at 49

r points using the same basis set functions as described above. In these calculations, a Hartree–Fock single determinant was used as the reference state and all the K shell orbitals were kept frozen. Typically, about 250 000 configuration state functions (CSF's) were generated to describe the correlation effect. The energy difference between the MCPF and SCF values, i.e., the correlation energies, were fitted by a polynomial $CE(r)$ of fourth order.

An analytical form for the reaction surface $V(r)$ including the zero point energy of the bath (adiabatic correction) and the correlation energy is given by the following expression:

$$V(\mathbf{r}) = V^{\text{SCF}}(\mathbf{r}) + CE(\mathbf{r}) + \text{ZPE}^{\text{SCF}}(\mathbf{r}). \quad (2.21)$$

The eigenstates of the reaction surface Hamiltonian were obtained by the vibrational MCSCF method.¹⁸ Typically 2000 vibrational configurations were generated, and both the expansion coefficients and the “harmonic exponents¹⁸” were optimized to minimize the total energy. The convergence of these expansions were checked by employing up to 10 000 configurations in selected points, and the numerical error of the vibrational energy was $< 1 \text{ cm}^{-1}$.

The SIRIUS²⁴ and ABACUS²⁵ program systems were used for the constrained geometry optimizations and the normal vibrational analysis. The program system MOLECULE/SWEDEN²⁶ was used for the MCPF calculations. The program system VIBR4²⁷ was used for the vibrational MCSCF calculations.

III. RESULTS AND DISCUSSIONS

A. The reaction surface, barrier energy, and geometries

The shape of the effective three-dimensional potential energy surface $V(r)$ in our calculations depends significantly on the adiabatic $\text{ZPE}^{\text{SCF}}(r)$ and the correlation energy $CE(r)$ terms in Eq. (2.21). For the sake of presentation we will emphasize the r_1 and r_2 dependence of the PES. For example, the SCF term $V^{\text{SCF}}(r)$ in Eq. (2.21) is represented in Fig. 1. At each point the variable r_3 (the O–O distance) has been adjusted to minimize the energy. Figure 2 portrays an analogous plot of the sum of the $V^{\text{SCF}}(r)$ and $CE(r)$. The analogous r_1 and r_2 dependence of the sum of all three contributions to the effective PES [i.e., $V(r)$ in Eq. (2.21)] is presented in Fig. 3.

The barrier energy of 10.6 kcal/mol at the SCF level of theory (Table I) is very close to the best SCF calculation previously reported (10.0 kcal/mol), see Table I. Inclusion of electron correlation (Fig. 2 and Table I) lowers the barrier by $\sim 40\%$. The calculated energy 6.3 kcal/mol is, however, much higher than MP2 and MP4 calculations of Schaefer and co-workers.⁸

To estimate how well the electron correlation effect is included in our MCPF calculations, we also carried out single reference CI_{SD} , using the Davidson's correction²⁸ for the effects of quadruple excitations. These methods generally give better results than calculations based on Møller–Plesset perturbation theory. The equilibrium and saddle point geometries optimized in the SCF calculations (see Fig. 4) were used in these calculations. The results are shown in Table II, together with the MCPF and the SCF values calculated at

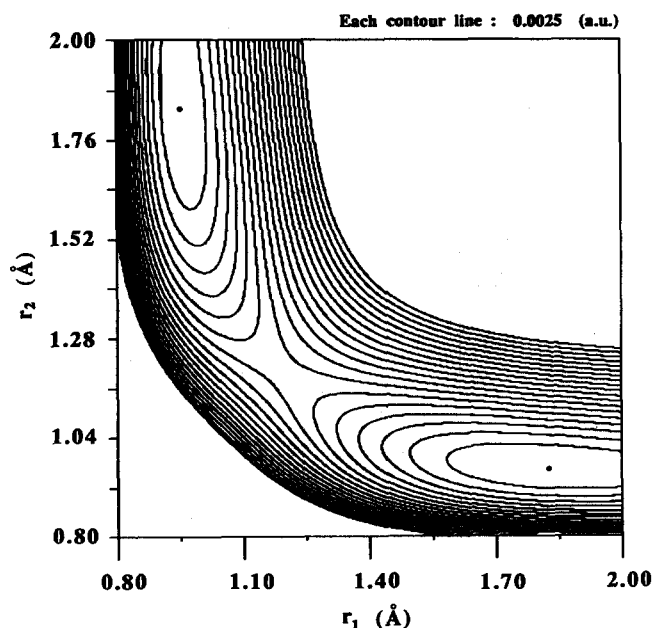


FIG. 1. A plot of $V^{\text{SCF}}(r)$ in Eq. (2.15) as a function of r_1 and r_2 . At each point (r_1, r_2) on the surface r_3 was optimized to minimize $V^{\text{SCF}}(r)$.

the same SCF geometries. In Table II, the correlation effect of the CI_{SD} and the $\text{CI}_{\text{SD}(Q)}$ calculations also lowers the barrier by $\sim 35\%$ and $\sim 40\%$, respectively, and the barrier height of the MCPF calculation is very close to the $\text{CI}_{\text{SD}(Q)}$ value.

The variation in barrier energy of the different calculations may also partly reflect how the geometries of the equilibrium point and saddle point are determined, and to what extent these geometries vary with electronic theoretical models, i.e., SCF, MP2, MP4, and MCPF.

In our calculations we determine these geometries di-

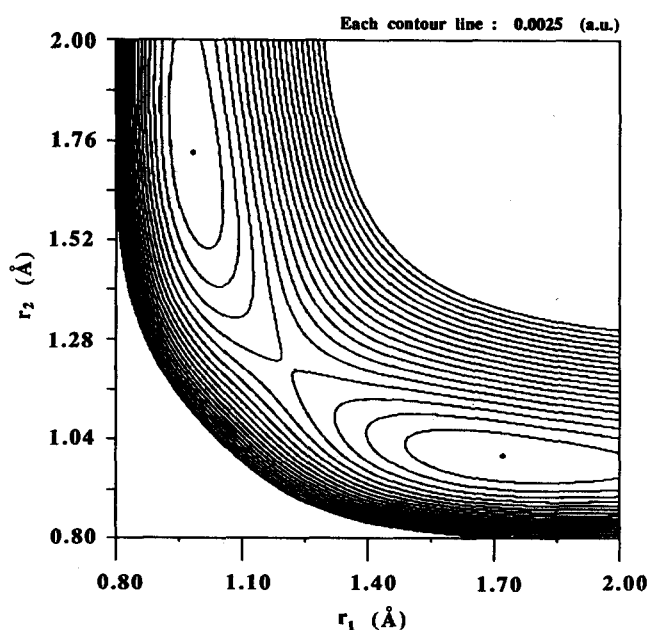


FIG. 2. A plot of $[V^{\text{SCF}}(r) + CE(r)]$ in Eq. (2.15) as a function of r_1 and r_2 . The r_3 coordinate was optimized in an analogous fashion to Fig. 1.

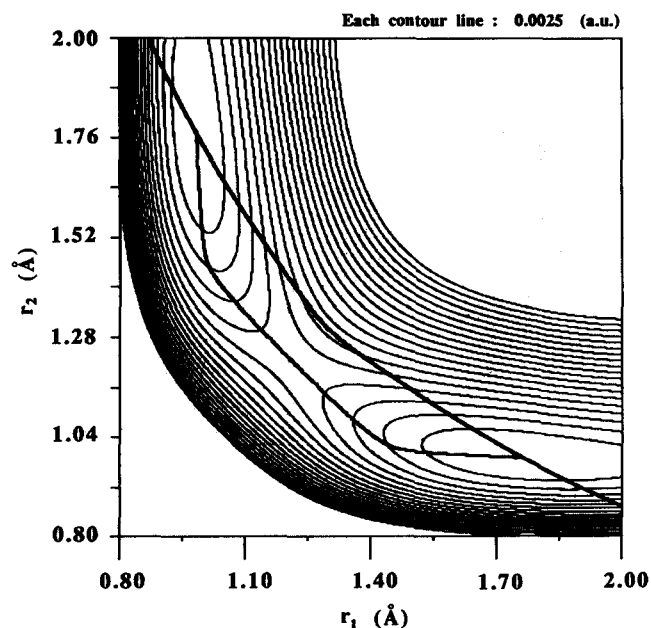


FIG. 3. A plot of $V(r)$ in Eq. (2.15) as a function of r_1 and r_2 . The r_3 coordinate was optimized in an analogous fashion to Fig. 1. The two bold lines in the figure are the MEP (minimum energy path) and the expectation value path EVP which are described in detail in the text.

rectly from a fitted form of the PES in Figs. 1 and 2. Thus, for equilibrium and saddle point geometries on the MCPF/SCF surface (Fig. 2), only r_1 , r_2 , and r_3 have been varied explicitly from the SCF level prediction of these geometries. However, other geometrical degrees of freedom have also been varied implicitly, since they are functions of r_1 , r_2 , and r_3 . This approximation makes efficient use of the electron correlation calculations, and yields an equilibrium geometry which is similar to that obtained in an MP2 calculation where the

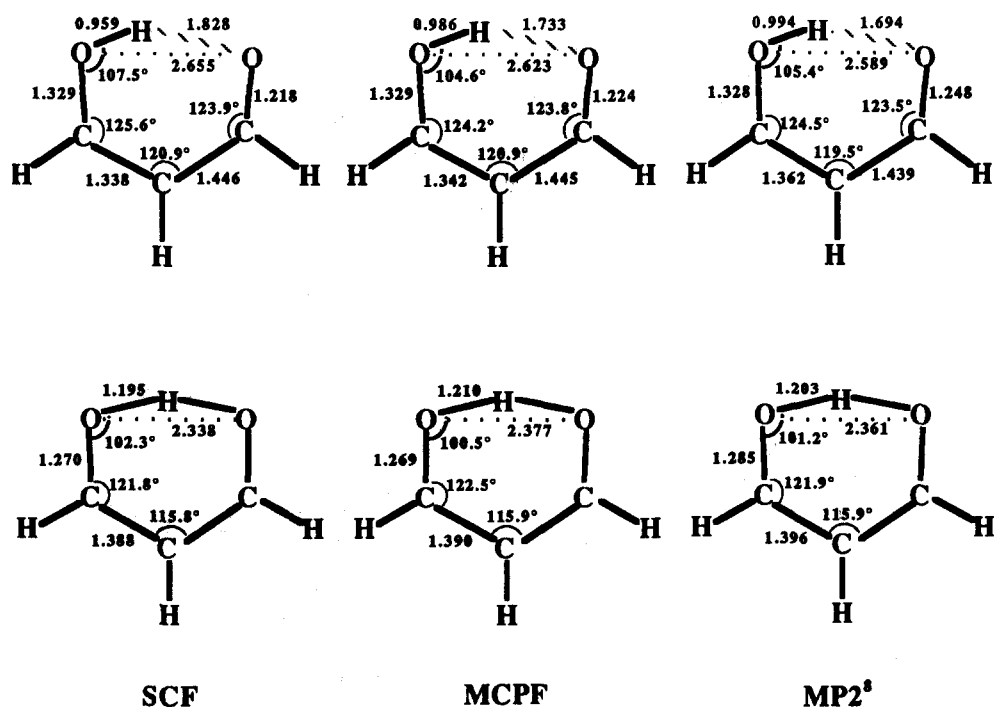


FIG. 4. Geometries for malonaldehyde of the equilibrium (upper) and the saddle point (lower) structures which have been calculated at the SCF, MCPF/SCF and MP2 (Ref. 8) levels.

TABLE I. A comparison of various calculations of the total energy and the proton transfer barrier height for malonaldehyde.

	Total energy (a.u.)	Barrier height (kcal/mol)
This work		
SCF	- 265.328 119	10.6
MCPF	- 265.994 678	6.3
Previous work ^a		
SCF (DZ + P)	- 265.697 88	10.0
MP2 (6-31G ^{**})	- 266.418 51	3.6
MP4 (6-31G ^{**})	...	4.3

^a Frish *et al.*, Ref. 8.

geometry was fully optimized.⁸ Apparently, the coordinates r_1 , r_2 , and r_3 are more dramatically altered when electron correlation effects are taken into account.

The various geometries are shown in Fig. 4 in which the equilibrium structure is portrayed on top of each structure, while the saddle point is represented on the bottom. Our r_1 , r_2 , and r_3 values in the MCPF/SCF calculation are similar to the optimized MP2 calculations. As noted previously, when electron correlation is included, the hydrogen bond distance is altered significantly from the SCF geometry.

It is important to note that the inclusion of electron correlation (Fig. 2) also significantly alters the shape of the PES, which plays an important role in determining the magnitude of the tunneling splitting and most probable proton tunneling path, see below. Making the MCPF calculation at numerous r_1 , r_2 , and r_3 geometries emphasizes the most important correction to the PES surface, while making efficient use of the most expensive portion of the electronic calculation.

TABLE II. A comparison with MCPF and CI calculations of the total energy and the proton transfer barrier height for malonaldehyde at the SCF geometries (Fig. 4).

Method	Total energy (a.u.)	Barrier height (kcal/mol)
CI _{SD}	-265.893 309	6.9
CI _{SD(Q)} ^a	-265.981 327	6.2
MCPF	-265.993 894	6.1
SCF	-265.328 119	10.6

^aThe total energy and the barrier height are estimated by the Davidson's correction (Ref. 28) i.e., $E_{\text{CI}_{\text{SD}(Q)}} = E_{\text{CI}_{\text{SD}}} + (\text{the Davidson's correction})$.

B. Tunneling splittings

We have calculated the vibrational wave functions and energies for the lower excited vibrational states associated with the reaction surface Hamiltonian model. The results are extremely sensitive to the PES employed as summarized by Table III. A large (H/D) isotope effect is observed, see below for further discussion. Our estimate for the tunneling splitting (MCPF surface with adiabatic corrections in Table III) is about a factor of 2 lower than experiment. In contrast, Miller and co-workers overestimate the splitting by about a factor of 3,⁷ employing a two-dimensional surface and a different procedure for electron correlation.

The magnitude of the tunneling splitting in Table III is related to the barrier height. Indeed, even one-dimensional treatments for MA give similar tunneling splittings (if O-H stretching motion is arbitrarily chosen as the reaction coordinate).^{5,6,10}

Nevertheless, the simple rough correlation of the tunneling splitting and barrier height is in contrast to the complex character of the proton transfer process that is uncovered by directly examining the vibrational wave function in the following section.

C. Vibrational wave functions and tunneling paths

As an introduction to the discussion of the "path" of proton transfer in MA it is useful to consider the definition of the intrinsic reaction path IRC, which was described in Sec. I. An analogous path in the three-dimensional reaction sub-

TABLE III. Tunneling splitting (cm^{-1}) for the ground vibrational state of malonaldehyde.

	Tunneling splitting		Barrier height (kcal/mol)
	H	D ₁ -MA	
This work			
MCPF surface with adiabatic correction	9	0.7	7.1
SCF surface	0.3	0.0	10.6
MCPF surface with no adiabatic correction	19	1.6	6.3
2D reaction surface ^a	60	...	4.3
Experimental value ^b	21	3	...

^aCarrington and Miller, Ref. 7.

^bWilson and co-workers, Ref. 10.

space is the steepest descent path in mass-weighted internal coordinates, see Appendix 2. We denote this path as MEP (minimum energy path) in the following discussion. Note that the definition of our MEP is somewhat different from that of the IRC.^{14(a)-14(c)} (The true IRC is defined only in mass-weighted Cartesian coordinates.) The MEP for MA is portrayed in Fig. 3. The MEP is the steepest descent path that passes through the saddle point and terminates at the equilibrium geometries. As stated above, in heavy-light-heavy systems the reasonable tunneling path (using a one-dimensional picture) can deviate significantly from the MEP.

The extent of deviation from the MEP for MA is nicely demonstrated in Fig. 5. The non-bold lines in Fig. 5 are contours of the ground vibrational nuclear probability distribution of MA in the reaction surface description. As expected, the nuclear probability distribution function $|\Phi(\mathbf{r})|^2$ of the ground state is highly peaked near the equilibrium geometry. Figure 5 is plotted on the same axes as Fig. 3. One of the bold lines in Fig. 5 is the MEP. It is interesting to note that the probability for symmetric ($r_1 = r_2$) geometries is not peaked near the MEP. In other words, there is no tendency for the reaction to pass through the classical transition state.^{5,6} This is emphasized in the window in Fig. 5 which is a blow-up of the region enclosed by a dotted line.

In order to explore further the dependence of the nuclear probability on coordinates \mathbf{r} of the PES, we have calculated two types of effective vibrational paths, i.e., an expectation value path EVP and a maximal probability path. The expectation value path is defined as follows. First, we introduce new coordinates, ρ_1 , ρ_2 , and ρ_3 ;

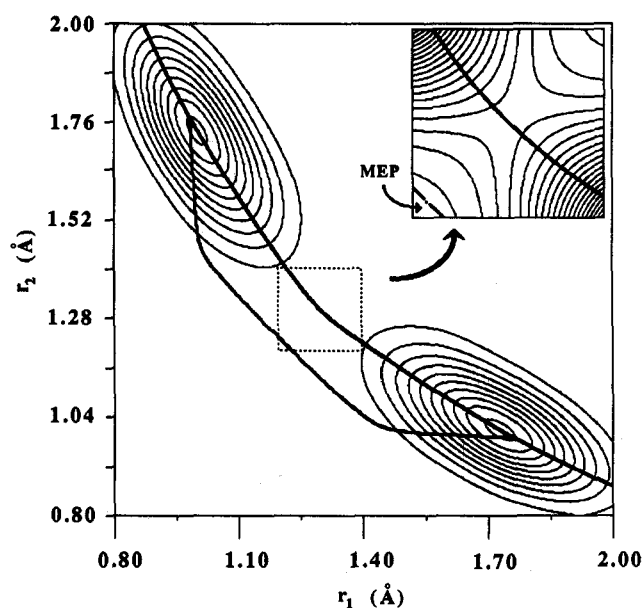


FIG. 5. Contour plots of the nuclear probability of the ground state vibrational wave function of the reaction surface (PES), see the text. The axis system and the bold line in the main part of the figure are identical to Fig. 3, and the equal spacing in an arbitrary unit was used. The upper right corner is an expansion of the dotted square region of the main part of the figure. The contours spacings in the expanded region is 20 times smaller than the spacing for the main figure, see the text for further detail.

$$\rho_1 \equiv r_1 - r_2, \quad (3.1a)$$

$$\rho_2 \equiv r_1 + r_2, \quad (3.1b)$$

$$\rho_3 \equiv r_3. \quad (3.1c)$$

Second, in terms of these coordinates a curvilinear path is calculated from Eq. (3.2);

$$\langle \rho_2(\rho_1) \rangle = \frac{\int |\Phi(\rho_1, \rho_2, \rho_3)|^2 \rho_2 d\rho_2 d\rho_3}{\int |\Phi(\rho_1, \rho_2, \rho_3)|^2 d\rho_2 d\rho_3}, \quad (3.2a)$$

$$\langle \rho_3(\rho_1) \rangle = \frac{\int |\Phi(\rho_1, \rho_2, \rho_3)|^2 \rho_3 d\rho_2 d\rho_3}{\int |\Phi(\rho_1, \rho_2, \rho_3)|^2 d\rho_2 d\rho_3}. \quad (3.2b)$$

The significance of this path is most obvious for $\rho_1 = 0$ (C_{2v} geometry), which falls on a line 45° from the r_1 axis on Fig. 5. The EVP intersects the 45° line at the averaged ρ_2 value of the nuclear probability distribution function $|\Phi(\mathbf{r})|^2 d\mathbf{r}$ (for the constraint $\rho_1 = 0$), see Eq. (3.2a). Away from the $\rho_1 = 0$ line, the EVP corresponds to the averaged geometry ρ_2 for chosen $\rho_1 = 0$ ($r_1 - r_2$) value. Thus, the EVP is a curved line of averaged nuclear positions for constrained displacement along ρ_1 . The path qualitatively indicates the most probable path of proton tunneling. This path is shown in the main part of Fig. 5 as the bold line. Note that the EVP is much less curved, and deviates significantly from the MEP. The difference is especially dramatic in the region of the PES portrayed in the window in Fig. 5.

More recently, we have been studying a maximal probability path for the nuclear wave function. This path is calculated from a hypersurface given by the negative of the probability $|\Phi(\mathbf{r})|^2$, which has valleys at the most probable geometries in Fig. 5. The saddle point on this surface is the most probable structure of C_{2v} geometry. The steepest descent path from the saddle point to the valleys defines a path of maximal probability for the vibrational wave function, in analogy (topographically) to the definition of the MEP. Our calculated maximal probability path (not shown) is virtually identical to the EVP in Fig. 5.

The deviation between the MEP and the EVP is consistent with the expectations for heavy-light-heavy systems. This is most easily demonstrated in a mass-weighted coordinate system (consistent with the reaction surface Hamiltonian model). For the sake of presentation, we have reduced the three-dimensional surface we have developed for MA to two dimensions. Figure 6 shows our representation of the desired mass weighted surface. The mass-weighted coordinates q_1 and q_2 correspond roughly to $r_1 - r_2$ and $r_1 + r_2$, although the relationship is not simple (see Appendix 3). The highly curved bold line EQ-MCP-SP-MCP-EQ in Fig. 6 is the MEP. The nuclear displacements along the MEP are shown in an exaggerated representation in Fig. 7. The MEP passes through the equilibrium geometry (EQ), the point we denote by MCP (maximal curvature point) and the saddle point (SP). The initial motion along the MEP (EQ \rightarrow MCP) is primarily stretching motion between the two oxygen atoms. This is followed by proton motion between the oxygen atoms (MCP \rightarrow SP \rightarrow MCP).

It is interesting to note that the EVP path involves much less O-O motion than the MEP. The EVP passes through a symmetric geometry, i.e., an effective saddle point (ESP), which has a much larger O-O separation than the true sad-

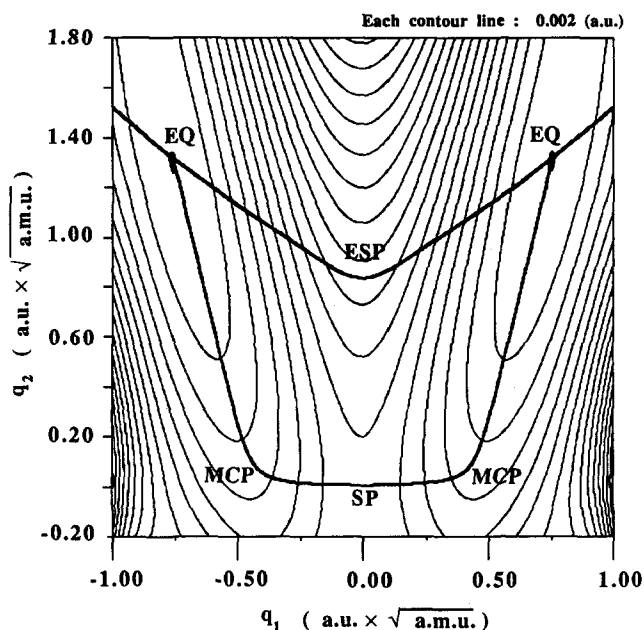


FIG. 6. A representation of the PES [$V(\mathbf{r})$] shown in Fig. 3, plotted in a transformed, mass-weighted, coordinate system, employing the new variables q_1 and q_2 , see the text for further details about this coordinate system and the abbreviations, EQ, ESP, MCP, and SP.

dle point. The EVP path is a compromise between potential energy which favors the MEP (lower barrier) and effective mass motion which would be minimized along a straight line path between the two EQ points.⁵⁻⁷

The interplay of potential energy and mass is nicely demonstrated in Fig. 8 in which the potential energies are plotted along the MEP and EVP. The steepest descent path from the SP is not defined beyond the equilibrium geometry in the direction away from the SP. For this portion of the MEP we used the recently developed gradient extremal path algorithm.^{18,19}

The MEP has (consistent with its definition) a significantly smaller barrier than the EVP. In contrast, the EVP barrier is much narrower at the base, since the motion along this path is less massive. Thus tunneling is much more effective along the EVP despite its large barrier energy. To further establish this point we undertook a one-dimensional vibrational calculation for the MEP and EVP. The calculat-

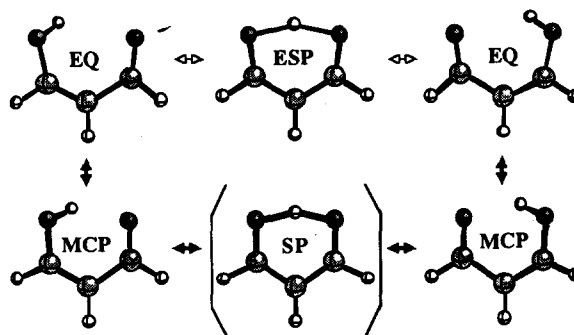


FIG. 7. The geometries of the various labeled points on Fig. 8. The abbreviations are defined in the text. The displacement of the saddle point geometry have been exaggerated by a factor of 2 in Fig. 7.

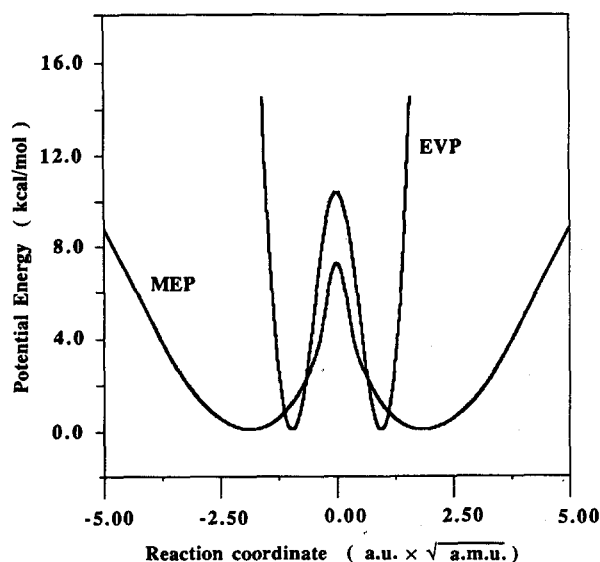


FIG. 8. The potential energy $V(r)$ dependence along the MEP and EVP in Fig. 8.

ed tunneling splittings, 0.0 and 0.3 cm^{-1} , respectively, further demonstrate the importance of the narrowness (light mass) of the EVP. In addition, the discrepancy of the one-dimensional calculation along the EVP for the splitting, and the full three-dimensional result (9 cm^{-1}) seems to demonstrate the necessity of a multidimensional approach.

D. Vibrational excited states

An examination of the excited vibrational states of malonaldehyde offers an opportunity to explore the dependence of the tunneling splitting or vibrational excitation. This leads, in principle, to insight into the multidimensional nature of proton tunneling in MA. In this section we consider two types of vibrational calculations which are denoted by fullspace and subspace. The level fullspace denotes a vibrational calculation involving the full $3N - 6$ (21 modes) surface. This has only been accomplished for the normal modes MA at the equilibrium geometry. The frequencies and characters of these modes are listed in the third and fourth column of Table IV. The level subspace is associated with the three-dimensional reaction surface (PES).

The adiabatic implementation of the reaction surface Hamiltonian method involves a separation of the $3N - 6$ vibrational degrees of freedom into $3N - 6 - m$ bath modes and m modes of the subspace (PES). The normal mode frequencies of the three-dimensional subspace are listed in the first column of Table IV.

With the exception of the 3950 cm^{-1} vibration ($\text{O}_2\text{-H}_1$ stretching) of the subspace, there is no simple relationship between the two types of normal modes. The 499 cm^{-1} mode is a combination of O-O stretching and an in-plane bending mode of the intramolecular hydrogen-bonded ring. The 2320 cm^{-1} mode is a complex motion involving displacements of many atoms of MA, inducing a significant $\text{O}_2\text{-H}_1\text{-O}_3$ in-plane bending.

The significant overlap of the normal modes of the subspace with the modes of the fullspace, and the similarity of

TABLE IV. Vibrational normal modes at the SCF level of electronic calculation for malonaldehyde and the reaction surface subspace. The relationship of the normal modes of the subspace to the normal modes of the fullspace are indicated by arrows in the overlap column. The numerical value associated with each arrow is the magnitude of the vibrational overlap of the pair of modes connected by the arrow.

Subspace Frequencies (cm^{-1})	overlap	Fullspace Frequencies (cm^{-1})	Character ^a
		274 (A'') ^b	$\text{O}_3 = \text{C}_6$ ring bend
		293	$\text{O}_2\text{-O}_3$ stretch
	0.94	460 (A'')	$\text{C}_4 = \text{C}_5$ ring bend
		535	$\text{O}_2\text{-C}_4$ in-plane ring bend
		873 (A'')	$\text{H}_1\text{-O}_2$ ring bend
	0.28	897 (A'')	$\text{H}_8\text{-C}_5$ ring bend
		974	in-plane ring bend (mixture)
		1026	in-plane ring bend (mixture)
		1181 (A'')	$\text{H}_{7,8,9}\text{-C}_{4,5,6}$ ring bend
	0.29	1192 (A'')	$\text{H}_{7,8,9}\text{-C}_{4,5,6}$ ring bend
	0.28	1215	$\text{H}_8\text{-C}_5$ in-plane ring bend
		1389	$\text{H}_7\text{-C}_4$ in-plane ring bend
		1544	$\text{H}_9\text{-C}_6$ in-plane ring bend
	0.69	1556	$\text{O}_2\text{-H}_1\text{-O}_3$ in-plane ring bend
		1611	$\text{C}_4 = \text{C}_5$ in-plane ring bend
	0.49	1789	$\text{C}_5\text{-C}_6$ in-plane ring bend
		1898	$\text{O}_2\text{-C}_4$ in-plane ring bend
		3171	$\text{H}_3\text{-C}_6$ stretch
		3367	$\text{H}_7\text{-C}_4$ stretch
	0.99	3408	$\text{H}_9\text{-C}_5$ stretch
		3834	$\text{H}_1\text{-O}_2$ stretch
499			
2320			
3950			

^aThe atom numbers are defined in the diagram of malonaldehyde.

^b A'' signifies out-of-plane vibrational modes.

some of the frequencies, implies that an attempt to calculate the exact vibrational states of MA by the adiabatic reaction surface Hamiltonian approach would be inaccurate due to the neglect of the important diabatic coupling between the bath and subspace modes.

The excited vibrational states of the subspace (Table V) alone can be examined to gain further insight on the tunneling process. But, it should be emphasized that these states do not actually correspond to states of MA since the coupling between the subspace and the bath modes are treated adiabatically.

The first 16 vibrational levels of the subspace assigned to eight pairs of levels with the average frequencies and splittings listed in Table V for malonaldehyde and deuterated malonaldehyde ($\text{D}_1\text{-MA}$). The vibrational zero-point ener-

TABLE V. A list of the eight lowest pairs of exact wave function levels of the reaction surface subspace.

Quantum No.		Transition energy (cm^{-1})		Splitting (cm^{-1})	
v_1	v_2	H	D	H	D
0	0	0	0	9	0.7
1	0	318	308	28	4
2	0	644	648	58	13
3	0	996	1032	89	27
4	0	1399	1474	109	47
0	1	1378	993	24	1.2
1	1	1754	1338	82	8
2	1	2183	1731	143	28

gy for MA is 2482 cm^{-1} , while D_1 -MA has a zero-point energy of 1844 cm^{-1} . The results in Table V have been obtained for the MCPF/adiabatic PES. For this surface the normal modes frequencies are: $\nu_1 = 307$, $\nu_2 = 1346$, and $\nu_3 = 3420\text{ cm}^{-1}$ for MA and $\nu_1 = 294$, $\nu_2 = 986$, and $\nu_3 = 2470\text{ cm}^{-1}$ for D_1 -MA. These modes are analogous to, though not exactly the same as the normal modes calculated at the SCF level, see Table IV. Mode 1 is O–O stretching and in-plane ring bend in character, consistent with the minor H/D isotope effect on the transition energy of this mode.

The vibrational states that are summarized in Table V are exact eigenstates for the three-dimensional PES (subspace, but not for the fullspace). They correspond closely to overtone and combination states of the normal modes (see above) of this surface. Table V lists the assignment of the pairs of levels to states involving different numbers of vibrational quanta in the two lowest frequency normal modes of the subspace. It is interesting to note that for all levels above the lowest pair of states ($\nu_1 = 0$, $\nu_2 = 0$), the total vibrational energy (zero point energy plus transition energy) is actually greater than the barrier energy of the PES which is 7.1 kcal/mol (2483 cm^{-1}). The existence of pairs of levels (each with a splitting) is a consequence of the near adiabatic separation of the tunneling motion from mode 1 and mode 2. In simple terms, the tunneling splitting of the various excited levels in Table V is associated with a barrier in a pseudopotential along the tunneling coordinate.

Vibrational excitation of mode 1 increases the tunneling splitting monotonically as a function of vibrational energy (quanta). But, the tunneling splitting is highly mode specific. For example, if almost the same vibrational energy is deposited in mode 1 ($\nu_1 = 4$, $\nu_2 = 0$) as compared to mode 2 ($\nu_1 = 0$, $\nu_2 = 1$), a much larger tunneling splitting is observed for the energy in mode 1, see Table V.

Presumably, the trends in Table V result from both adiabatic and diabatic effects involving modes 1,2 and the tunneling coordinate since, as stated above, the tunneling process intimately involves all three degrees of freedom of the surface. It is interesting, however, to speculate how the dependence of tunneling splitting on vibrational excitation might be rationalized in terms of a crude adiabatic picture. For example, it can be shown, that as successive quanta are added to mode 1, the average O–O bond separation increases because of the anharmonicity of the potential. Would an increase in the O–O separation increase or decrease the tunneling splitting? A qualitative answer to this question is obtained by the results described above which are summarized in Fig. 6. As the O–O separation is increased, the EVP should tend: (i) to be more curved (longer) and (ii) to have a larger barrier. Both effects tend to decrease the tunneling splittings in contrast to the results of Table V.

This analysis ignores the potential role of rms (root-mean-square) amplitude of mode 1 which increases when this mode is excited. This will tend both to enhance and diminish tunneling because of the larger spread in O–O separations. But, if very short O–O separations are much more important (which one might infer from the PES in Fig. 6), then the net effect of increased amplitude would be to increase the tunneling splitting. (It is noted that the similar

results were reported by Sato and Iwata using a simple two-dimensional model surface.²⁹) This qualitative effect may be responsible for the trends in Table V, but a more rigorous approach would be necessary to verify this assumption.

E. Hydrogen/deuterium isotope effects

We have made calculations analogous to those described above for a monodeuterated form of MA. The ratio of tunneling splitting of the H and D molecules for the ground state vibrational level is 12 which is close to the experimental value 7. The calculated EVP (not shown) is very similar to the path for undeuterated MA (Fig. 3). This may suggest that the actual path in both cases is primarily a result of the shape of the PES and the fact that MA is a heavy–light–heavy systems.

The results in Table V demonstrate that the isotope effect on the tunneling splitting decreases as the tunneling splittings increase. This is consistent with the notion that the effective potential barrier to the tunneling for the vibrationally excited states decreases in the excited states. For simple models, the isotope effect decreases as the barrier height is decreased.

IV. SUMMARY AND CONCLUSIONS

Proton tunneling in malonaldehyde (MA) has been studied in a three-dimensional reaction surface Hamiltonian model. A new reaction PES has been calculated, and the tunneling splitting of the vibrational level associated with the PES is in reasonable agreement with the experimental value for MA. The vibrational wave function of the ground state has been analyzed to yield an effective tunneling path for the proton transfer. The path deviates significantly from the MEP. Vibrationally excited states of the reaction PES show larger tunneling splitting than the ground state, but splitting is highly vibrational mode specific. The calculated isotope effect on the tunneling splitting is smaller than the experimental value. A number of other aspects of the reaction surface Hamiltonian model for MA have been explored.

As discussed previously, the reaction surface Hamiltonian offers an accurate means for the calculation of tunneling splittings in medium size molecules. The method nicely accounts for the strong deviation of the tunneling path from the intrinsic reaction path, which is the starting point of simpler models for proton transfer. In addition, the formalism naturally allows for a detailed analysis of multidimensional tunneling effects in polyatomics.

ACKNOWLEDGMENTS

Acknowledgment is made to the National Science Foundation (Grant Nos. CHE-8251158 and CHE-8610809), to the Donors of the Petroleum Research Foundation (Grant No. 20288-AC6), and to the Minnesota Supercomputer Institute. The authors would like to thank Professor George Schatz and Professor Don Truhlar for illuminating discussions. All the calculations were carried out on a Cray-2 computer at the Minnesota Supercomputer center.

APPENDIX 1

The effective Hessian matrix in Eq. (2.20) and the minimum energy surface condition (2.10) are derived in this section. The starting point for the derivation is the potential energy in terms of the reaction coordinates \mathbf{r} and the normal coordinates of the bath \mathbf{Q} . The potential energy can be expanded as a Taylor's series around an arbitrary point on the reaction surface $\mathbf{S}(\mathbf{r}_0)$ as

$$V_{rQ}(\mathbf{r}, \mathbf{Q}) = V_{rQ}(\mathbf{r}_0, \mathbf{0}) + \mathbf{g}_r^T \Delta \mathbf{r} + \mathbf{g}_Q^T \mathbf{Q} + \frac{1}{2} \Delta \mathbf{r}^T \mathbf{H}_{rr} \Delta \mathbf{r} + \Delta \mathbf{r}^T \mathbf{H}_{rQ} \mathbf{Q} + \frac{1}{2} \mathbf{Q}^T \mathbf{H}_{QQ} \mathbf{Q}, \quad (\text{A1.1})$$

where \mathbf{g} , and \mathbf{H} are gradient vectors and Hessian matrices defined as

$$(\mathbf{g}_r)_k = \left(\frac{\partial V}{\partial r_k} \right)_{\mathbf{r}=\mathbf{r}_0}, \quad (\text{A1.2a})$$

$$(\mathbf{g}_Q)_\alpha = \left(\frac{\partial V}{\partial Q_\alpha} \right)_{\mathbf{r}=\mathbf{r}_0}, \quad (\text{A1.2b})$$

$$(\mathbf{H}_{rr})_{kl} = \left(\frac{\partial^2 V}{\partial r_k \partial r_l} \right)_{\mathbf{r}=\mathbf{r}_0}, \quad (\text{A1.2c})$$

$$(\mathbf{H}_{rQ})_{k\alpha} = \left(\frac{\partial^2 V}{\partial r_k \partial Q_\alpha} \right)_{\mathbf{r}=\mathbf{r}_0}, \quad (\text{A1.2d})$$

$$(\mathbf{H}_{QQ})_{\alpha\beta} = \left(\frac{\partial^2 V}{\partial Q_\alpha \partial Q_\beta} \right)_{\mathbf{r}=\mathbf{r}_0}. \quad (\text{A1.2e})$$

\mathbf{H}_{QQ} in Eq. (A1.2e) must be a diagonal matrix since \mathbf{Q} are normal coordinates;

$$(\mathbf{H}_{QQ})_{\alpha\beta} \equiv \omega_\alpha^2 \delta_{\alpha\beta}. \quad (\text{A1.3})$$

In addition, we consider a Taylor's expansion of the potential energy in terms of mass-weighted Cartesian coordinates;

$$V_X(\mathbf{X}) = V_X(\mathbf{X}_0) + \mathbf{g}_X^T(\mathbf{X}_0) \Delta \mathbf{X} + \frac{1}{2} \Delta \mathbf{X}^T \mathbf{H}_X(\mathbf{X}_0) \Delta \mathbf{X} + \dots, \quad (\text{A1.4a})$$

$$\mathbf{X}_0 \equiv \mathbf{S}(\mathbf{r}_0). \quad (\text{A1.4b})$$

The chain rule of differentiation can be used to obtain the relation between \mathbf{g} and \mathbf{H} in the two different coordinate systems;

$$(\mathbf{g}_X)_i = \frac{\partial F_k}{\partial X_i} (\mathbf{g}_r)_k + \frac{\partial Q_\alpha}{\partial X_i} (\mathbf{g}_Q)_\alpha, \quad (\text{A1.5a})$$

$$\begin{aligned} (\mathbf{H}_X)_{ij} &= \frac{\partial F_k}{\partial X_i} \frac{\partial F_l}{\partial X_j} (\mathbf{H}_{rr})_{kl} + \frac{\partial F_k}{\partial X_i} \frac{\partial Q_\alpha}{\partial X_j} (\mathbf{H}_{rQ})_{k\alpha} \\ &+ \frac{\partial Q_\alpha}{\partial X_j} \frac{\partial F_k}{\partial X_i} (\mathbf{H}_{rQ})_{k\alpha} + \frac{\partial Q_\alpha}{\partial X_i} \frac{\partial Q_\beta}{\partial X_j} (\mathbf{H}_{QQ})_{\alpha\beta} \\ &+ \frac{\partial^2 F_k}{\partial X_i \partial X_j} (\mathbf{g}_r)_k + \frac{\partial^2 Q_\alpha}{\partial X_i \partial X_j} (\mathbf{g}_Q)_\alpha + \phi_{ij}, \end{aligned} \quad (\text{A1.5b})$$

where ϕ are the contributions from rotational and translational degrees of freedom.

Up to this point in the derivation, the choice of the bath coordinate \mathbf{Q} is not unique. Here, we impose the following condition on \mathbf{Q} :

$$\frac{\partial r_k}{\partial X_i} \frac{\partial Q_\alpha}{\partial X_j} = \frac{\partial r_k}{\partial X_i} L_{i\alpha} = 0. \quad (\text{A1.6})$$

To obtain the condition that defines the minimum energy surface and the bath frequencies, we extract \mathbf{g}_Q and \mathbf{H}_{QQ} from Eq. (A1.5) by projecting out other terms. For this purpose, we first define the projection operator $(\mathbf{1} - \mathcal{P})$ which projects out the (infinitesimal) translational, rotational and \mathbf{r} components from an arbitrary vector as;

$$(\mathbf{1} - \mathcal{P}) \equiv (\mathbf{1} - \mathcal{P}^{(r)}) (\mathbf{1} - \mathcal{P}^{(R)}) (\mathbf{1} - \mathcal{P}^{(T)}). \quad (\text{A1.7})$$

The explicit form of the $\mathcal{P}^{(R)}$ and $\mathcal{P}^{(T)}$ operators are analogous to $\mathcal{P}^{(r)}$ which is defined by Eq. (2.12). The use of a projection operator for rotations is based on the first order approximation of a linear relation between rotational coordinates and mass-weighted Cartesian coordinates, such as in the use of the Eckart criteria.³⁰ It is easy to show that the following relations are satisfied when $(\mathbf{1} - \mathcal{P})$ is operated to $\partial F_k / \partial \mathbf{X}$, $\partial Q_\alpha / \partial \mathbf{X}$, and ϕ ;

$$(\mathbf{1} - \mathcal{P})_{ij} \frac{\partial F_k}{\partial X_j} = 0, \quad (\text{A1.8a})$$

$$(\mathbf{1} - \mathcal{P})_{ij} \frac{\partial Q_\alpha}{\partial X_j} = L_{i\alpha}, \quad (\text{A1.8b})$$

$$(\mathbf{1} - \mathcal{P})\phi = 0. \quad (\text{A1.8c})$$

Using the projection operator in Eq. (A1.7), \mathbf{g}_Q and \mathbf{H}_{QQ} can be extracted from Eq. (A1.5) as follows:

$$(\mathbf{1} - \mathcal{P})\mathbf{g}_X = \mathbf{L}\mathbf{g}_Q, \quad (\text{A1.9a})$$

$$(\mathbf{1} - \mathcal{P})\mathbf{H}_{\text{eff}}(\mathbf{1} - \mathcal{P}) = \mathbf{L}\mathbf{H}_{QQ}\mathbf{L}^T, \quad (\text{A1.9b})$$

$$(\mathbf{H}_{\text{eff}})_{ij} = (\mathbf{H}_X)_{ij} - \frac{\partial^2 F_k}{\partial X_i \partial X_j} (\mathbf{g}_r)_k - \frac{\partial^2 Q_\alpha}{\partial X_i \partial X_j} (\mathbf{g}_Q)_\alpha. \quad (\text{A1.9c})$$

A sufficient condition to construct the minimum energy surface ($\mathbf{g}_Q = \mathbf{0}$) is obtained from Eq. (A1.9a) as

$$(\mathbf{1} - \mathcal{P})\mathbf{g}_X = \mathbf{0}. \quad (\text{A1.10})$$

When the minimum surface condition (A1.10) is satisfied on the reaction surface $\mathbf{S}(\mathbf{r})$, the last term in Eq. (A1.9c) becomes zero and \mathbf{H}_{eff} can be written as

$$(\mathbf{H}_{\text{eff}})_{ij} = (\mathbf{H}_X)_{ij} - \frac{\partial^2 F_k}{\partial X_i \partial X_j} (\mathbf{g}_r)_k. \quad (\text{A1.11})$$

If one defines \mathbf{H}'_{eff} as;

$$\mathbf{H}'_{\text{eff}} \equiv (\mathbf{1} - \mathcal{P})\mathbf{H}_{\text{eff}}(\mathbf{1} - \mathcal{P}), \quad (\text{A1.12})$$

Eq. (A1.9b) can be rewritten as

$$(\mathbf{H}'_{\text{eff}})_{ij} L_{j\alpha} = \omega_\alpha^2 L_{i\alpha}. \quad (\text{A1.13})$$

The three relations (A1.11), (A1.12), and (A1.13) are three parts of Eq. (2.20). Equation (2.10) is given by Eq. (A1.10).

APPENDIX 2

The effective steepest descent path in Fig. 3 (MEP) can be calculated as follows. The Lagrangian in internal coordinates can be written as

$$\begin{aligned} \mathcal{L} &= \hat{T} - \hat{V} = \frac{1}{2} \mathbf{P}^T \mathbf{G}(\mathbf{r}) \mathbf{P} - V(\mathbf{r}) \\ &= \frac{1}{2} \dot{\mathbf{r}}^T \mathbf{G}^{-1}(\mathbf{r}) \dot{\mathbf{r}} - V(\mathbf{r}). \end{aligned} \quad (\text{A2.1})$$

Since the derivatives of \mathcal{L} with respect to \mathbf{r} and $\dot{\mathbf{r}}$ are calculated as

$$\frac{\partial \mathcal{L}}{\partial \dot{\mathbf{r}}} = \mathbf{G}^{-1}(\mathbf{r})\dot{\mathbf{r}}, \quad (\text{A2.2a})$$

$$\frac{\partial \mathcal{L}}{\partial \mathbf{r}} = -\frac{\partial V(\mathbf{r})}{\partial \mathbf{r}} \equiv -\mathbf{F}(\mathbf{r}). \quad (\text{A2.2b})$$

The Lagrange equation is determined as

$$\frac{d}{dt}[\mathbf{G}^{-1}(\mathbf{r})\dot{\mathbf{r}}] = -\mathbf{F}(\mathbf{r}). \quad (\text{A2.3})$$

If the following initial conditions are applied;

$$\dot{\mathbf{r}} = \mathbf{0} \text{ at } t = 0, \quad (\text{A2.4a})$$

Eq. (A2.3) can be written approximately as

$$d\mathbf{r} = -C\mathbf{G}(\mathbf{r})\mathbf{F}(\mathbf{r}), \quad (\text{A2.4b})$$

where C is a "small time constant."^{14(a)}

APPENDIX 3

The transformation from internal coordinates to orthonormalized mass-weighted coordinates (Fig. 6) can be obtained as follows. The kinetic energy in internal coordinates is expressed as

$$2\hat{\mathbf{T}} = \dot{\mathbf{r}}^T \mathbf{G}^{-1}(\mathbf{r})\dot{\mathbf{r}}. \quad (\text{A3.1})$$

If one introduces a unitary matrix \mathbf{u} which diagonalizes the matrix \mathbf{G} ;

$$\mathbf{G}\mathbf{u} = \mathbf{u}\boldsymbol{\epsilon}, \quad (\text{A3.2})$$

Eq. (A3.1) can be written as

$$2\hat{\mathbf{T}} = \dot{\mathbf{r}}^T (\mathbf{u}\boldsymbol{\epsilon}^{-1}\mathbf{u}^T)\dot{\mathbf{r}} = (\boldsymbol{\epsilon}^{-1/2}\mathbf{u}^T\dot{\mathbf{r}})^T (\boldsymbol{\epsilon}^{-1/2}\mathbf{u}^T\dot{\mathbf{r}}). \quad (\text{A3.3})$$

Introducing a new set of coordinates \mathbf{q} satisfies

$$\dot{\mathbf{q}} \equiv \boldsymbol{\epsilon}^{-1/2}\mathbf{u}^T\dot{\mathbf{r}}, \quad (\text{A3.4})$$

leads to the following kinetic energy form;

$$\hat{\mathbf{T}} = \frac{1}{2}\dot{\mathbf{q}}^T\dot{\mathbf{q}}. \quad (\text{A3.5})$$

The coordinates \mathbf{q} can be obtained by solving

$$\mathbf{q}(\mathbf{r}) = \int_{r_0}^{\mathbf{r}} \boldsymbol{\epsilon}^{-1/2}(\mathbf{r})\mathbf{u}^T(\mathbf{r})d\mathbf{r}. \quad (\text{A3.6})$$

\mathbf{q} in Eq. (A3.6) are the generalized mass weighted coordinates. The \mathbf{G} matrix in that basis is a unit matrix at every point, in space.

¹G. Karlström, H. Wennerström, B. Jönsson, S. Forsen, J. Almlöf, and B. Roos, *J. Am. Chem. Soc.* **97**, 4188 (1975).

²A. D. Isaacson and K. Morokuma, *J. Am. Chem. Soc.* **97**, 4453 (1975).

³S. Kato, H. Kato, and K. Fukui, *J. Am. Chem. Soc.* **99**, 684 (1977).

⁴H. Ogoshi and K. Nakamoto, *J. Chem. Phys.* **45**, 3113 (1966).

⁵(a) E. M. Fluder and J. R. de la Vega, *J. Am. Chem. Soc.* **100**, 5265 (1978); (b) J. R. de la Vega, *Acc. Chem. Res.* **15**, 185 (1982); (c) J. Bicerano, H. F. Schaefer III, and W. H. Miller, *J. Am. Chem. Soc.* **105**, 2550 (1983).

⁶M. Y. Ovchinnikova, *Chem. Phys.* **36**, 85 (1979); V. K. Babamov and R. A. Marcus, *J. Chem. Phys.* **74**, 1790 (1978); B. C. Garrett, D. G. Truhlar, A. F. Wagner, and T. H. Dunning, Jr., *ibid.* **78**, 4400 (1983); D. K. Bondi,

J. N. L. Connor, B. C. Garrett, and D. G. Truhlar, *ibid.* **78**, 5981 (1983); D. G. Truhlar, A. D. Isaacson, and B. C. Garrett, *Theory of Chemical Reaction Dynamics*, edited by M. Baer (CRC, Boca Raton, 1985), Vols. 1 and 2.

⁷T. Carrington and W. H. Miller, *J. Chem. Phys.* **84**, 4364 (1986).

⁸M. J. Frisch, A. C. Scheiner, H. F. Schaefer, and J. S. Binkley, *J. Chem. Phys.* **82**, 4194 (1985); J. S. Binkley and M. J. Frisch, *Chem. Phys. Lett.* **126**, 1 (1986).

⁹J. S. Hutchinson, *J. Phys. Chem.* **91**, 4495 (1987).

¹⁰S. L. Baughcum, Z. Smith, E. B. Wilson, and R. W. Duerst, *J. Am. Chem. Soc.* **106**, 2260 (1984); P. Turner, S. L. Baughcum, S. L. Coy, and Z. Smith, *ibid.* **106**, 2265 (1984); S. L. Baughcum, R. W. Duerst, W. F. Rowe, Z. Smith, and E. B. Wilson, *ibid.* **103**, 6296 (1981).

¹¹C. J. Seliskar and R. E. Hoffman, *J. Mol. Spectrosc.* **88**, 30 (1981); **96**, 146 (1982).

¹²D. Firth, H. P. Trommsdorff, and P. F. Barbara, *Chem. Phys.* (to be published).

¹³For a recent review on the static and time resolved spectroscopy of polyatomic molecules that undergo intramolecular proton transfer see; P. F. Barbara, P. K. Walsh, and L. E. Brus, *J. Phys. Chem.* **93**, 29 (1989).

¹⁴(a) K. Fukui, *J. Phys. Chem.* **74**, 4161 (1970); (b) also in *The World of Quantum Chemistry*, edited by R. Daudel and B. Pullman (Dordrecht, Netherlands, 1974); (c) *Accts. Chem. Res.* **14**, 368 (1981); see also (d) I. Shavitt, Theoretical Chemistry Laboratory Report; No. WIS-AEC-23, University of Wisconsin, 1959; (e) R. A. Marcus, *J. Chem. Phys.* **45**, 4493 (1966), and **49**, 2610 (1968).

¹⁵W. H. Miller, N. C. Handy, and J. E. Adams, *J. Chem. Phys.* **72**, 99 (1980); W. H. Miller, in *The Theory of Chemical Reaction Dynamics*, edited by D. C. Clary (Reidel, Dordrecht, 1986), p. 27; and references therein.

¹⁶L. Hofacker, *Z. Naturforsch., Teil A* **18**, 607 (1963); R. A. Marcus, *J. Chem. Phys.* **43**, 1598 (1965), **45**, 2630, 4493 (1966), and **46**, 9591 (1967); D. G. Truhlar, *ibid.* **53**, 2041 (1970); D. G. Truhlar and A. Kuppermann, *J. Am. Chem. Soc.* **93**, 1840 (1971); D. G. Truhlar and B. G. Garrett, *J. Phys. Chem.* **83**, 1052 (1979); S. Kato and K. Morokuma, *J. Chem. Phys.* **73**, 3900 (1980).

¹⁷For a recent discussion see, M. Page and J. W. McIver, Jr., *J. Chem. Phys.* **88**, 922 (1988).

¹⁸N. Shida, J. E. Almlöf, and P. F. Barbara, *Theor. Chim. Acta* **76**, 7 (1989).

¹⁹D. K. Hoffman, R. S. Nord, and K. Rudenberg, *Theor. Chim. Acta* **69**, 265 (1986); P. Jørgensen, H. J. Aa. Jensen, and T. Helgaker, *ibid.* **73**, 55 (1988).

²⁰If the same suffix arises more than once in each term and it is not explicitly denoted at the opposite side of the equation, then the suffix is assumed to be a dummy variable (running suffix).

²¹E. B. Wilson, Jr., J. G. Decius, and P. C. Cross, *Molecular Vibrations* (McGraw-Hill, New York, 1955), Chap. 4.

²²D. P. Chong and S. R. Langhoff, *J. Chem. Phys.* **84**, 5606 (1986); The original CPF method is R. Ahlrichs, P. Scharf, and C. Ehrhardt, *ibid.* **82**, 890 (1985).

²³The orbital exponents and contraction coefficients used were those given in; F. B. Duijneveldt, *IBM J. Res. Dev.* **1971**, 945.

²⁴SIRIUS is a second order SCF-MCSCF program system developed by H. J. Aa Jensen, H. Ågren, and P. Jørgensen.

²⁵ABACUS is a property program system of SIRIUS for geometry optimizations and normal vibrational analysis. In ABACUS, analytic nuclear gradients vectors and Hessian matrices are calculated from SCF-MCSCF wave functions. The program code was developed by T. Helgaker, P. Jørgensen, and H. J. Aa Jensen.

²⁶MOLECULE/SWEDEN is a vectorized SCF-MCSCF-CI-(M)CPF program system developed by P. E. M. Siegbahn, C. W. Bauschlicher, Jr., B. Roos, P. R. Taylor, A. Heiberg, J. Almlöf, S. R. Langhoff, and D. P. Chong.

²⁷VIBR4 is a vibrational MCSCF program system developed by N. Shida.

²⁸E. R. Davidson, in *The World of Quantum Chemistry*, edited by R. Daudel and B. Pullman (Dordrecht, Netherlands, 1974).

²⁹N. Sato and S. Iwata, *J. Chem. Phys.* **89**, 2932 (1988).

³⁰C. Eckart, *Phys. Rev.* **47**, 552 (1935).